37th AIAA Plasmadynamics and Lasers Conference, Jun 5–8 2006, San Francisco CA

Plasma-Based Hypersonic Flow Control

Jonathan Poggie*

Air Force Research Laboratory, Wright-Patterson AFB, OH 45433-7512 USA

Progress is reported in an ongoing numerical study of the application of plasma actuator technology to high-speed flow control. As part of this project, a three-dimensional computer code has been written to solve, simultaneously, the fluid conservation laws, the charged particle continuity equations, and the Poisson equation for the electric potential. In past work, the code was applied to the evaluation of DC glow discharge actuators for hypersonic boundary layer control. Here the numerical model is extended and applied to RF glow discharge devices. Preliminary calculations have reproduced many of the documented features of the α-mode, or low current density RF discharge mode. Ongoing work addresses the behavior of RF discharges in boundary layer flows. An additional study has been carried out of a Mach 14 compression ramp flow using a reduced order model. The effects near reattachment of both steady and unsteady actuation near separation were evaluated. The most beneficial effects of steady actuation were obtained with surface heating and with an upstream-directed body force. With control applied, the shear layer was seen to reattach on the ramp with a slightly shallower angle, leading to reduced velocity and temperature gradients at reattachment, and consequently a reduction in the peak heat flux. Unsteady actuation was seen to introduce a region of hot, slow fluid, similar to a turbulent boundary layer structure, that convected through the reattachment zone, temporarily altering the shear layer in a manner similar to that observed with steady actuation. Future work will address this problem using the high-fidelity model.

I. Introduction

Interest in electromagnetic control of high-speed flows dates to the mid-1950s, when the problem of hypersonic atmospheric entry was first being explored. Given the high temperatures in the shock layer around a reentry vehicle, and the concomitant ionization and electrical conductivity, it was natural to consider exploiting electromagnetic effects for flow control. Interest in large-scale plasma-aerodynamics has waxed and waned several times in the intervening decades, with the initial enthusiasm eventually damped each time by the realities of the weight and complexity of high-strength magnets and power conditioning equipment.

Because of the nonlinear scaling of the weight of this equipment with actuator size, small-scale actuators are not prohibitively heavy. For example, a magnet capable of generating a field of order 1 T over a meter extent weighs on the order of tons (e.g., a medical MRI machine), whereas the same field strength applied over a centimeter can be obtained with a small permanent magnet. Thus small-scale plasma actuators are currently considered to be a promising means of flow control for application in both propulsion and external aerodynamics.

Over the past few years, the Air Force Research Laboratory Computational Sciences Center (AFRL/VAAC) has been developing numerical tools to study the possibility of local flow control with electromagnetic tech-

*Senior Aerospace Engineer, AFRL/VAAC, Bldg. 146 Rm. 225, 2210 Eighth St. Associate Fellow AIAA.

niques. Because non-neutrality near electrode surfaces is an essential feature of glow discharge behavior, a prototype computer code is being developed to model space charge effects.

In initial work, this code was applied to two-dimensional simulations of DC glow discharges in the normal glow regime in the absence of bulk gas flow.[1,2] Two-dimensional discharges were also explored with finite electrodes in the abnormal glow regime.[3] This work was later extended to three dimensions, with the effects of varying background pressure and applied magnetic field examined.[4,5] Control of a two-dimensional, low Reynolds number airfoil flow was explored,[2,4] but was found to be relatively ineffective. Greater success was obtained for a Mach 5 flat plate boundary layer flow,[2,4,5] with reasonable comparison to the experimental data of Menart *et al.*[6] obtained in Ref. 5.

Recent work has avoided the computational cost of high-fidelity discharge modeling by employing a simplified model of the mechanical and thermal energy inputs introduced by a plasma actuator. In particular, a Mach 14 compression ramp flow has been studied, and locations have been identified where a modest power input can result in significant structural changes to the flow.[7]

The point of this work has been to study plasma actuator modeling at two levels: a level with computationally intensive detailed modeling and a level with simplified modeling emphasizing the fluid dynamic response to the actuation. The present paper continues on this path, including high-fidelity modeling of an RF discharge (Sec. III) and unsteady actuation of the Mach 14 compression ramp flow (Sec. IV).

II. Methods

A three-dimensional computer code has been written to solve the bulk-flow conservation laws, drift-diffusion equations, and Poisson equation in an implicit, loosely-coupled fashion. Several numerical techniques, including proper evaluation of the source terms and implicit procedures, have proven to be critical to successful high-fidelity simulations.

A. Physical Model

The conservation of mass, momentum, and energy for the overall gas is expressed as:

$$\frac{\partial \rho}{\partial t} + \nabla \cdot (\rho \mathbf{u}) = 0 \tag{1}$$

$$\frac{\partial}{\partial t}(\rho \mathbf{u}) + \nabla \cdot (\rho \mathbf{u}\mathbf{u} - \boldsymbol{\Sigma}) = \mathbf{f} \tag{2}$$

$$\frac{\partial \mathcal{E}}{\partial t} + \nabla \cdot (\mathbf{u}\mathcal{E} - \boldsymbol{\Sigma} \cdot \mathbf{u} + \mathbf{Q}) = \mathbf{f} \cdot \mathbf{u} + S \tag{3}$$

where ρ is the gas density, $\mathbf{u}$ is its velocity, $\boldsymbol{\Sigma}$ is the total stress tensor, $\mathcal{E} = \rho(\epsilon + u^2/2)$ is the total fluid energy, ϵ is the internal energy, and $\mathbf{Q}$ is the heat flux. The total stress tensor $\boldsymbol{\Sigma}$ is given by the usual constitutive equation for a Newtonian fluid and the heat flux $\mathbf{Q}$ follows Fourier's heat conduction law. The source terms on the right hand sides of the conservation equations include a body force $\mathbf{f}$ and a dissipative energy source S. Simplified models of these sources terms will be discussed later in Sec. IV.

In the detailed plasma model, the body force is $\mathbf{f} = \rho_c \mathbf{E} + \mathbf{j} \times \mathbf{B}$ and the total energy delivered to the fluid by electromagnetic effects is $\mathbf{f} \cdot \mathbf{u} + S = \mathbf{E} \cdot \mathbf{j}$. The mass density, the charge density, and the total current density are found by summing over all species: $\rho = \Sigma_s m_s n_s$, $\rho_c = \Sigma_s q_s n_s$, and $\mathbf{j} = \Sigma_s q_s n_s \mathbf{v}_s$, where m is the mass per particle, n is the species number density, q is the charge per particle, and $\mathbf{v}$ is the species velocity.

Neglecting acceleration terms and diffusion due to temperature gradients, the particle and momentum conservation equations for each species can be combined to obtain a drift-diffusion model:

$$\frac{\partial n_s}{\partial t} + \nabla \cdot \{n_s \left[\mathbf{u} + s_s \mu_s \mathbf{M}^s \cdot (\mathbf{E} + \mathbf{u} \times \mathbf{B})\right]\} = \nabla \cdot (D_s \mathbf{M}^s \cdot \nabla n_s) + \omega_s \tag{4}$$

where s_s is the sign of q_s, and the tensor $\mathbf{M}^s$ is defined as:

$$M_{ij}^s = \frac{1}{1+\mu_s^2 B^2}\left(\delta_{ij} + \mu_s^2 B_i B_j + s_s \mu_s \epsilon_{ijk} B_k\right) \tag{5}$$

The dot product in Eq. (4) corresponds to summation on the second index of M_{ij}.

For the present work, two species of charged particles are considered (ions and electrons, denoted below by subscript i and e), and the charged particle generation rate is taken to have the form:

$$\omega_{i,e} = \alpha \Gamma_e - \beta n_i n_e \tag{6}$$

where α is the ionization coefficient, β is the recombination coefficient, and Γ_e is the magnitude of the electron flux relative to the bulk gas flow. The RF discharge calculations presented in this paper were carried out for nitrogen gas. Data for the mobilities, diffusion coefficients, ionization coefficient, and recombination coefficient were taken from Ref. 8.

The electric potential is determined from the Poisson equation:

$$\nabla^2 \phi = -\rho_c / \epsilon_0 \tag{7}$$

where ϵ_0 is the permittivity of free space, and the electric field is found from $\mathbf{E} = -\nabla\phi$.

Conventional no-slip wall conditions and inlet/outlet boundary conditions were used for the fluid equations. The boundary conditions for the RF discharge required some modification from those used in past work on DC discharges. When the normal component of the electric field was directed away from an electrode (anode-like behavior), the normal component of the ion flux was assumed to be zero. For the opposite case of cathode-like behavior, the normal component of the electron flux was found from the relation $\mathbf{\Gamma}_e \cdot \mathbf{n} = -\gamma \mathbf{\Gamma}_i \cdot \mathbf{n}$, where γ is the secondary emission coefficient, $\mathbf{n}$ is a unit normal vector, and the species fluxes $\mathbf{\Gamma}_{i,e}$ were computed using one-sided, second-order spatial differences. The potential at the right electrode was taken to be zero. The potential at the left electrode was determined by solving an auxiliary ordinary differential equation for the external circuit (see Fig. 1b):

$$\dot{V} + V/(RC) = I/C \tag{8}$$

where

$$I = I_C + I_D = -\iint (\mathbf{j} + \epsilon_0 \frac{\partial \mathbf{E}}{\partial t}) \cdot \mathbf{n}\, dA \tag{9}$$

is the sum of the conduction and displacement currents at the right electrode in the plasma solution, R is the external resistance, C is the external capacitance, V is the voltage drop across the resistor and capacitor, $V_L = V - V_s$ is the voltage at the left electrode, and V_s is the driving voltage source. Equation (8) was solved in a similar manner to the time integration of Eqs. (1)–(4), to be described next.

B. Numerical Methods

The conservation laws were solved using approximately-factored, implicit schemes, related to those developed by Beam and Warming,[9] Pulliam,[10] and Surzhikov and Shang.[8] Applying the standard transformation from physical coordinates (x, y, z) to grid coordinates (ξ, η, ζ), the conservation equations (1)–(4) can be written in the form:

$$\frac{\partial \overline{U}}{\partial t} + \frac{\partial \overline{E}}{\partial \xi} + \frac{\partial \overline{F}}{\partial \eta} + \frac{\partial \overline{G}}{\partial \zeta} = \frac{\partial \overline{E}_v}{\partial \xi} + \frac{\partial \overline{F}_v}{\partial \eta} + \frac{\partial \overline{G}_v}{\partial \zeta} + \overline{S} \tag{10}$$

where, for example, $\overline{U} = U/J$, $\overline{E} = (\xi_x E + \xi_y F + \xi_z G)/J$, and for the fluid conservation laws $U = [\rho, \rho u_x, \rho u_y, \rho u_z, \mathcal{E}]^T$. (Here J is the Jacobian of the grid transformation.)

Writing Eq. (10) as $\partial \overline{U}/\partial t = R$, and discretizing in time, we have:

$$(1+\theta)\overline{U}^{n+1} - (1+2\theta)\overline{U}^{n} + \theta \overline{U}^{n-1} = \Delta t R^{n+1} \tag{11}$$

where $\theta = 0$ for an implicit Euler scheme and $\theta = 1/2$ for a three point backward scheme. We introduce subiterations such that $\overline{U}^{n+1} \rightarrow \overline{U}^{p+1}$, with $\Delta\overline{U} = \overline{U}^{p+1} - \overline{U}^{p}$. The right hand side R^{n+1} is linearized in the standard 'thin layer' manner. Collecting the implicit terms on the left hand side, and introducing approximate factoring and a subiteration time step $\Delta\hat{t}$ gives an equation set of the form:

$$\mathcal{L}_\xi \mathcal{L}_\eta \mathcal{L}_\zeta \Delta\overline{U} = -\frac{\Delta\hat{t}}{1+\theta}\left\{\frac{(1+\theta)\overline{U}^{p} - (1+2\theta)\overline{U}^{n} + \theta\overline{U}^{n-1}}{\Delta t} - R^{p} - D_e\overline{U}^{p}\right\} \tag{12}$$

where $\mathcal{L}_\xi$, $\mathcal{L}_\eta$, and $\mathcal{L}_\zeta$ are implicit spatial difference operators.

For the bulk fluid conservation laws, the scheme employs the implicit and explicit damping operators described by Pulliam.[10] The explicit damping operator D_e uses a nonlinear blend of second- and fourth-order damping.[11] The spatial derivatives are evaluated using second order central differences.

For the drift-diffusion equations, no damping is used. Instead, these equations are discretized in space using a second-order upwind scheme based on the convection-drift velocity $\mathbf{V}_s = \mathbf{u} + s_s\mu_s\mathbf{M}^s \cdot (\mathbf{E} + \mathbf{u} \times \mathbf{B})$. The minmod limiter is employed. A second-order, upwind method was also applied when calculating the species fluxes present in the source terms. (See the discussion of the charged particle generation term in Refs. 5, 8.)

The Poisson equation is solved using an approximately factored implicit scheme, adapted from the approach described by Holst.[12,13] Applying the usual transformation of coordinates, the three-dimensional Poisson equation (7) can be written in the form:

$$\frac{\partial\phi}{\partial\tau} = \frac{\partial\overline{E}}{\partial\xi} + \frac{\partial\overline{F}}{\partial\eta} + \frac{\partial\overline{G}}{\partial\zeta} - \overline{S} \tag{13}$$

where the left hand side is an artificial time term that motivates an iterative procedure for driving the right hand side towards zero. We write $\Delta\phi/\Delta\tau = L\phi^{p+1}$, where $\Delta\phi = \phi^{p+1} - \phi^{p}$. We then linearize the right hand side using the standard 'thin layer' approach, introduce $\alpha = 1/\Delta\tau$, an over-relaxation parameter ω, and approximate factoring. This gives:

$$\mathcal{L}_\xi \mathcal{L}_\eta \mathcal{L}_\zeta \Delta\phi = \omega\alpha^{-1} L\phi^{p} \tag{14}$$

The spatial derivatives are evaluated using second-order central differences. A cyclic variation of the pseudo-time parameter is used in order to accelerate convergence.

The fluid equations, the drift-diffusion equations, and the Poisson equation are solved in a loosely-coupled fashion inside a subiteration loop intended to drive $\Delta\overline{U}$ and $\Delta\phi$ toward zero. Typically 1-3 overall subiterations are employed, with 10-1000 iterations of the Poisson solver within each overall subiteration.

Due to the disparate time scales involved in the fluid dynamic and electromagnetic phenomena occurring in these problems, calculations can be costly in computer time. Efforts have been made to improve the speed of the computations. In the implementation of the factorized schemes, multi-level parallelism is exploited by using vectorization, multi-threading with OpenMP commands,[14] and multi-block decomposition implemented through MPI commands.[15] Further, the code is set up to run either in a time-accurate mode or with independent time-steps for the different physics modules to accelerate convergence.

III. RF Discharge

In previous work, detailed, three-dimensional calculations of the behavior of DC glow discharges were carried out. Here, this work is extended to RF discharges. The working gas was nitrogen at 670 Pa and 293 K. The secondary emission coefficient was taken to be $\gamma = 0.1$. The effects of gas flow and heating are neglected in this preliminary work.

For the case considered here, the computational domain was $51 \times 51 \times 51$ points, distributed over a cube which was 20 mm on a side. The computational grid is shown in Fig. 1a. The electrodes were taken to

be located in the $x = 0$ and $x = 20$ mm planes, and a zero gradient condition was imposed on the other sidewalls of the domain.

The computations were carried out with 200 time steps per cycle, and continued for several hundred cycles. Time integration was carried out with second order accuracy, with three applications of the plasma solver per time step (three subiterations).

The circuit configuration is shown in Fig. 1b. The electrodes are assumed to be in contact with the ionized gas; there is no insulating coating. A 10 MHz voltage source with 1 kV peak-to-peak amplitude drives the discharge and an external load consisting of a 3.33 pF capacitor in parallel with a 3.0 kΩ resistor.

Time-series plots of the potential at the left electrode V_L, the conduction current at the right electrode I_C, and the displacement current at the right electrode I_D are shown in Fig. 1c. The sign convention is such that positive current is from right electrode to left; see Eq. (9). Despite the presence of the external circuit elements, the potential at the left electrode closely follows the driving signal. The conduction current appears as a series of pulses, which occur when the slug of electron gas touches the electrode. The primary charge carriers are electrons, but the negative conduction current that appears between pulses is primarily created by ion motion into the electrode. The displacement current is seen to be a slightly distorted sine wave, out of phase with the driving voltage source.

A three-dimensional perspective view corresponding to the condition $V_L = -500$ V is shown in Fig. 1d. Note that negligible conduction current occurs at the right electrode at this stage, and also the spreading of the current lines as they approach the left electrode. The mass of electrons is moving toward the right electrode at this stage. (See Ref. 16, Sec. 1.5, for a description of an RF discharge model in which the electron gas oscillates back and forth within a stationary background of ion gas.)

Centerline profiles are shown in Figs. 2a-d, and x-y-sections through the solution are shown in Figs. 2e-h, for corresponding stages in one cycle of the driving voltage source. In these plots, the ion number density distribution shows essentially no variation through the cycle, whereas the electrons are seen to move back and forth across the gap. Note the cathode-like behavior of both electrodes: the number density of electrons tends to be less than that of the ions on both sides. The peak in the ion density at the center reflects a weak average ion flux toward the electrodes, generated by diffusion and the average electric field.

Peak conduction current at the right electrode occurs at about 20% phase, close to the conditions depicted in Figs. 2b and 2f. The large positive current (out of the right electrode) at this stage represents the flow of electrons into the right electrode as the mass of electron gas touches the electrode.

Given the relatively low current densities observed in the solution (~ 100 A/m^2 in the plasma center), and the apparent lack of a significant effect of secondary emission (no local maximum in the ion density in the sheath region), the solution is judged to be representative of the low current density α-mode.[16]

IV. Compression Ramp Flow

The computational cost of high-fidelity modeling (as in Sec. III) was avoided by applying a simplified plasma actuator model to the study of the control of a separated compression ramp flow. The baseline flow was taken to be the Mach 14 compression ramp flow originally studied by Holden and Moselle.[17] The ramp configuration consisted of an initial flat plate of length $L = 439$ mm and width $W = 610$ mm mounted parallel to the freestream, followed by a second plate, inclined to the freestream by an angle of $\theta = 24°$. The freestream conditions, upstream of the leading edge shock, were $M = 14.1$ and $\mathrm{Re}_L = 1.04 \times 10^5$.

For comparison to the experimental data, three dimensional calculations were carried out on $202 \times 60 \times 60$ and $404 \times 120 \times 120$ grids. A detailed discussion of this configuration and the associated boundary conditions is given in Ref. 7. The skin friction distribution is shown in Fig. 3a, and the temperature field is shown in Fig. 3b. These plots illustrate the three-dimensional separated flow pattern present in the vicinity of the corner. The results of the comparison with experiment are summarized in Fig. 3c, which compares the predicted heat transfer coefficient (Stanton number $C_h = q_w/[\rho_\infty U_\infty (H_\infty - H_w)]$) on the model centerline to the experimental data of Holden and Moselle. The separation location is seen to be accurately predicted on the finer grid, but the peak heat transfer rate is somewhat over-predicted, and occurs slightly upstream

of that observed in the experimental data. Similar results have been observed in previous computational studies of this flow.[18–23]

Phenomenological models of the dissipative heating S and body force $\mathbf{f}$ were considered [See Eqs. (2)-(3)], and their effects on the flow were evaluated. The volumetric heating model had the form:

$$S = \frac{Q}{\pi^{3/2} a^3} \exp\left(-\frac{r^2}{a^2}\right) \tag{15}$$

and was added to the total energy equation (3). Here the variable r represents the distance from the center of the heating, and Q is the total energy deposited by the source term. The applied body force had the analogous form:

$$\mathbf{f} = \frac{2Q}{U_\infty \pi^{3/2} a^3} \exp\left(-\frac{r^2}{a^2}\right) \mathbf{e}_x \tag{16}$$

and was added to the momentum equation (2), with $\mathbf{f} \cdot \mathbf{u}$ added to the total energy equation (3). Note that this source term integrated over all space has the value $2Q/U_\infty$, so that the net mechanical power delivered to the fluid is comparable to the heating specified in Eq. (15). The surface heating model had the form:

$$q_w = \frac{Q}{\pi a^2} \exp\left(-\frac{r^2}{a^2}\right) \tag{17}$$

and was applied as a boundary condition. Here the variable r represents the distance along the wall from the center of the heating, and the surface integral of q_w over the boundary gives the total energy deposited Q.

A series of exploratory studies of the effect of steady volumetric heating, body forces, and surface heating were carried out on a $202 \times 60 \times 60$ grid. The intensity of energy deposition was determined by the values $Q = 100$ W and $a = 5$ mm, and the 'actuators' were located on the centerline, halfway down the initial flat plate ($L/2 = 220$ mm). The volumetric sources were centered 8 mm from the wall. For the cases with five actuators, the spanwise locations were $z = 0$, $z = \pm 105$ mm, and $z = \pm 205$ mm.

Selected results for the effect of the heating-based control cases are shown in Fig. 3d. (Because of the varying wall and total temperatures, a modified heat transfer coefficient $C_h = q_w/[\rho_\infty U_\infty H_\infty]$ is shown.) The peak heat transfer rate downstream of reattachment is seen to be reduced for both cases shown, with only moderate changes to the rest of the profile. Some heat transfer penalty is incurred near the actuator location.

Case	x/L	C_f	$C_h = \frac{q_w}{\rho_\infty U_\infty H_\infty}$	C_p
Baseline	1.28	2.25×10^{-2}	2.05×10^{-2}	0.741
Surface Heating	1.30	1.58×10^{-2}	1.73×10^{-2}	0.668
Surface Heating x 5	1.32	1.77×10^{-2}	1.80×10^{-2}	0.731
Volumetric Heating	1.29	1.86×10^{-2}	1.90×10^{-2}	0.707
Volumetric Heating x 5	1.30	1.97×10^{-2}	1.91×10^{-2}	0.741
Downstream force	1.27	2.59×10^{-2}	2.19×10^{-2}	0.731
DS Force & Vol. Heating (50 W each)	1.28	2.15×10^{-2}	2.03×10^{-2}	0.722
Upstream Force	1.30	1.83×10^{-2}	1.86×10^{-2}	0.723
Upward Force	1.32	1.70×10^{-2}	1.69×10^{-2}	0.709
Downward Force	1.27	2.80×10^{-2}	2.27×10^{-2}	0.766

Table 1. Conditions at peak reattachment heating ($z/L = 0$): effect of control.

A summary of the effect at the peak heating location for a number of steady control cases is given in Table 1. The most significant reductions in peak heat transfer were obtained with upstream and upward forces, and with surface and volumetric heating. The heat transfer integrated over the surface of the plate $q_{\rm net} = \iint \mathbf{q}_w \cdot \mathbf{n}\, dS$ was also computed to determine the net effect of each control case. Although significant local decreases in heat transfer occurred with control, the net heat load remained nearly the same. The maximum change in total heat transfer was slightly over 1%, which occured for the heating cases with five actuators.

A study of unsteady actuation was carried out next, motivated by the results of the steady actuation computations. Large values for total power delivered were chosen to insure that a strong, visible effect was present. The total dissipative energy addition was $Q = 2$ kW and the mechanical work was $Q = 0.5$ kW. The force vector was oriented outward and upstream, at an angle of $\pi/4$ from the wall. Time modulation was introduced with the following form:

$$m(t) = \frac{1}{2}\left(1 - \cos 2\pi f t\right) \tag{18}$$

with a modulation frequency of $f = 25$ kHz. The source terms in Eqs. (15)-(16) were multiplied by $m(t)$ for these calculations. In contrast to the heat transfer rate specified in the steady actuation cases, Eq. (17), here the 'electrode' was maintained at a constant temperature of 1000 K.

A top view of the plate, with contours of wall heat transfer rate, is shown in Fig. 4. Results from six stages through the cycle of the driving signal are shown in sub-figures 4a-f. The actuator is seen to introduce a region of hot, slow fluid, similar in nature to a δ-scale structure in a turbulent boundary layer, that convects downstream. As each such structure passes through the reattachment zone, it is seen to reduce the heat transfer rate on its centerline, but introduce local hot spots to either side. After the structure convects past, the reattachment region begins to return its previous state. There appears to be a pair of counter-rotating, streamwise vortices associated with the actuation.

A side view of the reattachment region, with temperature contours, is shown in Fig. 5. The phase associated with each sub-figure is the same as in Fig. 4. The temperature contours illustrate the structure introduced by the actuation as it convects through the reattachment zone. As each structure convects through, it appears to lift up the hot entropy layer from the leading edge shock, and pull colder fluid from the corner flow into the region near the wall. This acts as a kind of insulation for the wall in the reattachment zone, reducing the peak heat transfer rate.

V. Summary and Conclusions

Over the past several years, a program has been underway to develop a capability to numerically simulate experiments with plasma actuators and evaluate their potential for flow control applications. As part of this project, a three-dimensional computer code has been written to solve, simultaneously, the fluid conservation laws, the charged particle continuity equations, and the Poisson equation for the electric potential. In past work, the code has been applied to the evaluation of DC glow discharge actuators for hypersonic boundary layer control. Here the numerical model is extended and applied to RF glow discharge devices. Preliminary calculations have reproduced many of the documented features of the α-mode, or low current density RF discharge mode. Ongoing work addresses the behavior of RF discharges in boundary layer flows.

An additional study has been carried out of a Mach 14 compression ramp flow using a reduced order model. The object of this work was to determine whether a moderate power input through a glow discharge actuator located upstream of separation could lead to structural changes in the flow. First, the effects of steady actuation were evaluated. The most beneficial effects were obtained with surface heating and with an upstream-directed body force. With control applied, the shear layer was seen to reattach on the ramp with a slightly shallower angle, leading to reduced velocity and temperature gradients at reattachment, and consequently a reduction in the peak heat flux.

Next, the effects of unsteady, periodic actuation were examined. The device was seen to introduce a region

of hot, slow fluid, similar to a turbulent boundary layer structure, that convected through the reattachment zone, temporarily altering the shear layer in a manner similar to that observed with steady actuation. Future work will address this problem using the high-fidelity model.

Acknowledgments

This project is sponsored in part by the Air Force Office of Scientific Research (monitored by J. Schmisseur and F. Fahroo), and by a grant of High Performance Computing time from the Department of Defense Major Shared Resource Center at the Army High Performance Computing Research Center (AHPCRC). The author would like to acknowledge helpful discussions of the present work with D. Gaitonde, R. Kimmel, J. Shang, and M. White.

References

[1]Poggie, J. and Sternberg, N., "Numerical Simulation of Glow Discharges for High-Speed Flow Control," AIAA Paper 2004-0177, American Institute of Aeronautics and Astronautics, Reston VA, January 2004.

[2]Poggie, J., "Numerical Exploration of Flow Control with Glow Discharges," AIAA Paper 2004-2658, American Institute of Aeronautics and Astronautics, Reston VA, June 2004.

[3]Poggie, J., "Implicit, Approximately-Factored, Upwind Scheme for Glow Discharge Modeling," *Computational Fluid and Solid Mechanics 2005*, edited by K. J. Bathe, Elsevier, Amsterdam, 2005, pp. 998–1000.

[4]Poggie, J., "Computational Studies of High-Speed Flow Control with Weakly-Ionized Plasma," AIAA Paper 2005-0784, American Institute of Aeronautics and Astronautics, Reston VA, January 2005.

[5]Poggie, J., "DC Glow Discharges: A Computational Study for Flow Control Applications," AIAA Paper 2005-5303, American Institute of Aeronautics and Astronautics, Reston VA, June 2005.

[6]Menart, J., Henderson, S., Atzbach, C., Shang, J., Kimmel, R., and Hayes, J., "Study of Surface and Volumetric Heating Effects in a Mach 5 Flow," AIAA Paper 2003-2262, American Institute of Aeronautics and Astronautics, June 2003.

[7]Poggie, J., "Plasma-Based Control of Shock-Wave / Boundary-Layer Interaction," AIAA Paper 2006-1007, American Institute of Aeronautics and Astronautics, Reston VA, January 2006.

[8]Surzhikov, S. T. and Shang, J. S., "Two-Component Plasma Model for Two-Dimensional Glow Discharge in Magnetic Field," *Journal of Computational Physics*, Vol. 199, 2004, pp. 437–464.

[9]Beam, R. and Warming, R., "An Implicit Factored Scheme for the Compressible Navier-Stokes Equations," *AIAA Journal*, Vol. 16, No. 4, 1978, pp. 393–402.

[10]Pulliam, T. H., "Implicit Finite-Difference Simulations of Three-Dimensional Compressible Flow," *AIAA Journal*, Vol. 18, No. 2, 1980, pp. 159–167.

[11]Jameson, A., Schmidt, W., and Turkel, E., "Numerical Solutions of the Euler Equations by a Finite Volume Method Using Runge-Kutta Time Stepping Schemes," AIAA Paper 81-1259, American Institute of Aeronautics and Astronautics, Reston, VA, 1981.

[12]Holst, T. L., "On Approximate Factorization Schemes for Solving the Full Potential Equation," NASA TM 110435, 1997.

[13]Holst, T. L., "Transonic Flow Computations Using Nonlinear Potential Methods," *Progress in Aerospace Sciences*, Vol. 36, 2000, pp. 1–61.

[14]Chandra, R., Dagum, L., Kohr, D., Maydan, D., McDonald, J., and Menon, R., *Parallel Programming in OpenMP*, Academic Press, San Diego, 2001.

[15]Gropp, W., Lusk, E., and Skjellum, A., *Using MPI: Portable Parallel Programming with the Message-Passing Interface*, The MIT Press, Cambridge, MA, 2nd ed., 1999.

[16]Raizer, Y. P., Shneider, M. N., and Yatsenko, N. A., *Radio-Freqency Capacitive Discharges*, CRC Press, Boca Raton, 1995.

[17]Holden, M. S. and Moselle, J. R., "Theoretical and Experimental Studies of the Shock Wave - Boundary Layer Interaction on Compression Surfaces in Hypersonic Flow," Tech. Rep. ARL 70-0002, Aerospace Research Laboratories, January 1970.

[18]Hung, C. M. and MacCormack, R. W., "Numerical Solutions of Supersonic and Hypersonic Laminar Compression Ramp Flows," *AIAA Journal*, Vol. 14, No. 4, 1976, pp. 475–481.

[19]Power, G. D. and Barber, T. J., "Analysis of Complex Hypersonic Flows with Strong Viscous/Inviscid Interaction," *AIAA Journal*, Vol. 26, No. 7, 1988, pp. 832–840.

[20]Rizzetta, D. and Mach, K., "Comparative Numerical Study of Hypersonic Compression Ramp Flows," AIAA Paper 89-1877, American Institute of Aeronautics and Astronautics, Reston, VA, June 1989.

[21]Rudy, D. H., Thomas, J. L., Kumar, A., Gnoffo, P. A., and Chakravarthy, S. R., "Computation of Laminar Hypersonic Compression-Corner Flows," *AIAA Journal*, Vol. 29, No. 7, 1991, pp. 1108–1113.

[22]Gaitonde, D. and Shang, J. S., "The Performance of Flux-Split Algorithms in High-Speed Viscous Flows," AIAA Paper 92-0186, American Institute of Aeronautics and Astronautics, Reston, VA, January 1992.

[23]Updike, G. A., Shang, J. S., and Gaitonde, D. V., "Hypersonic Separated Flow Control Using Magneto-Aerodynamic Interaction," AIAA Paper 2005-0164, American Institute of Aeronautics and Astronautics, Reston, VA, January 2005.

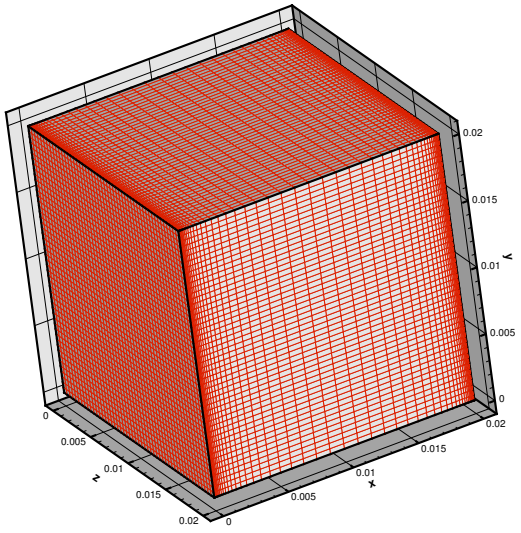

(a) Computational grid.

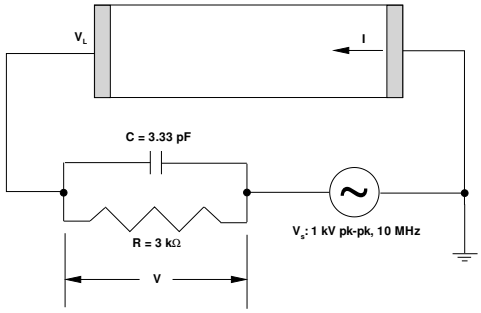

(b) Circuit configuration.

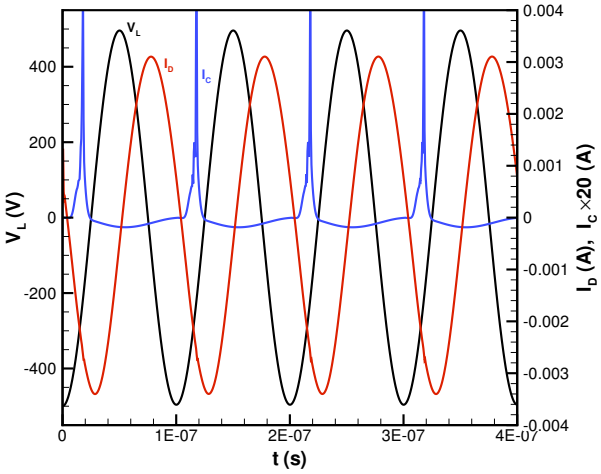

(c) Voltage at left electrode and current at right electrode.

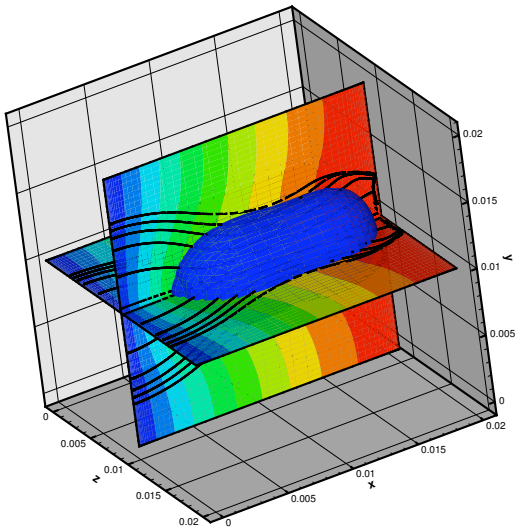

(d) Iso-surface $n_e = 1 \times 10^{14}$ m^{-3}, conduction current lines, electric potential (50 V intervals) at $V_L = -500$ V.

Figure 1. RF discharge calculations.

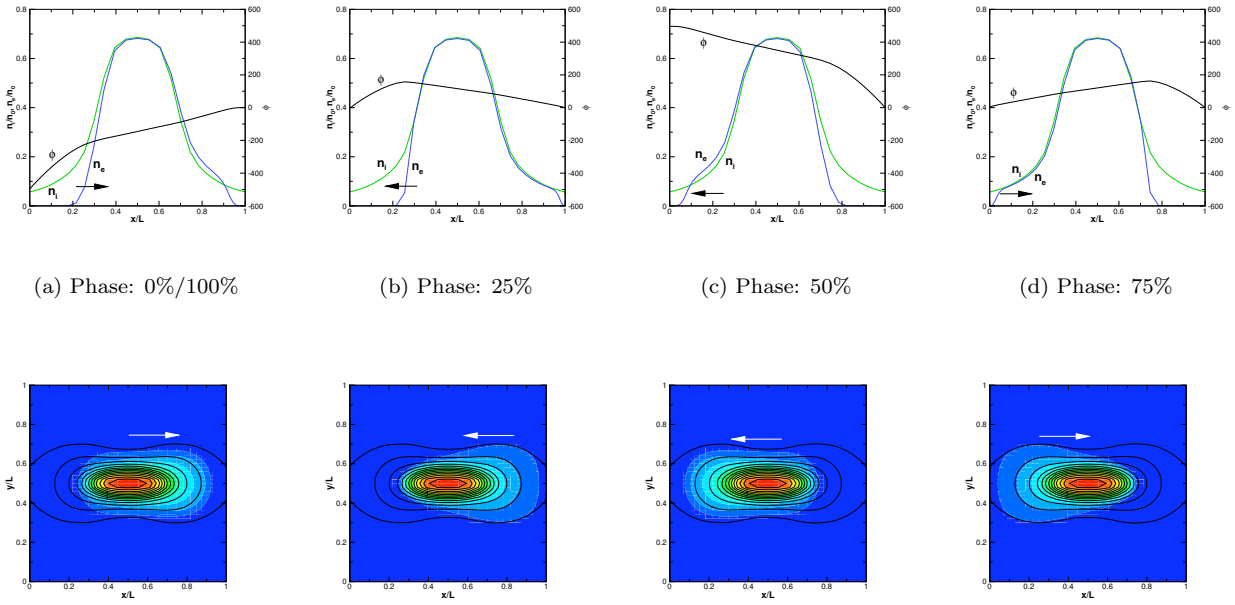

(a) Phase: 0%/100% (b) Phase: 25% (c) Phase: 50% (d) Phase: 75%

(e) Phase: 0%/100% (f) Phase: 25% (g) Phase: 50% (h) Phase: 75%

Figure 2. RF Discharge cycle. Centerline profiles of potential ϕ and number densities $n_{i,e}$. Center plane contour plots of ion (lines) and electron (colors) number density; contour interval 5×10^{14} $\mathbf{m}^{-3}$.

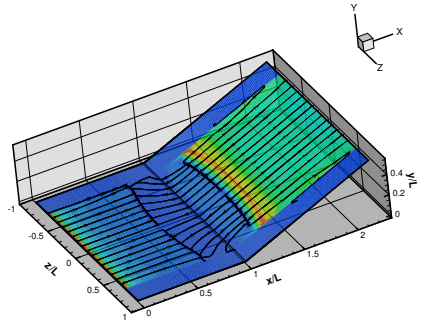

(a) Skin friction magnitude and trajectories, baseline flow.

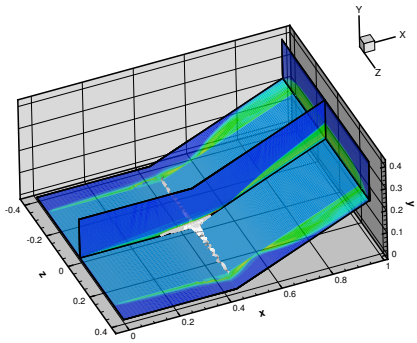

(b) Temperature field and selected stream ribbons, baseline flow.

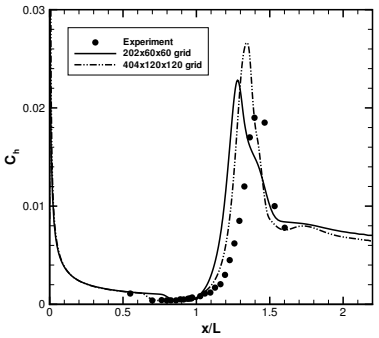

(c) Baseline flow validation: heat transfer coefficient on wall centerline.

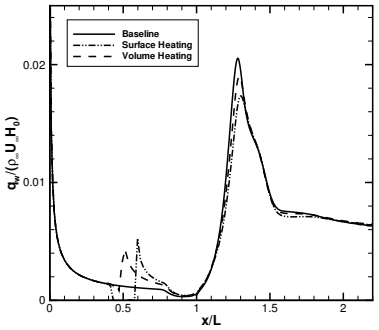

(d) Effects of control on wall heat transfer rate.

Figure 3. Results of three-dimensional computations of 24° ramp flow.

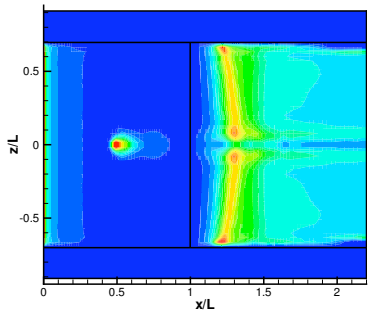

(a) Phase: 0%

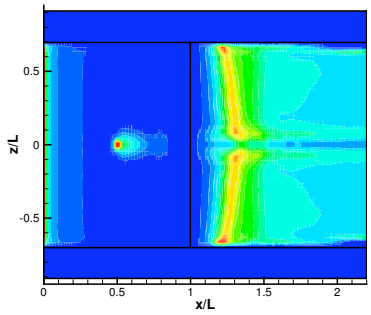

(b) Phase: 20%

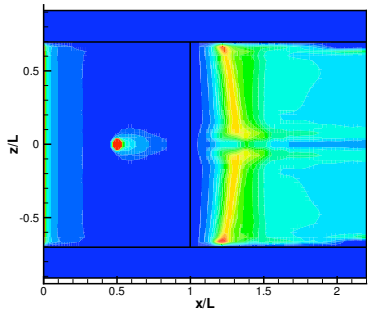

(c) Phase: 40%

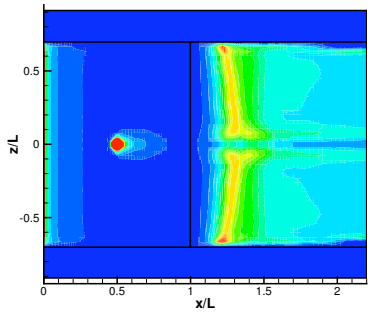

(d) Phase: 60%

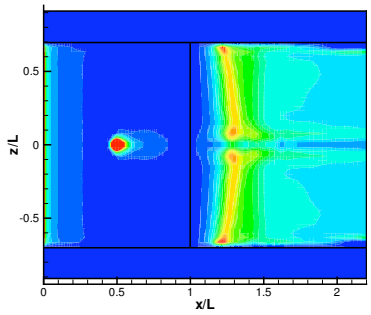

(e) Phase: 80%

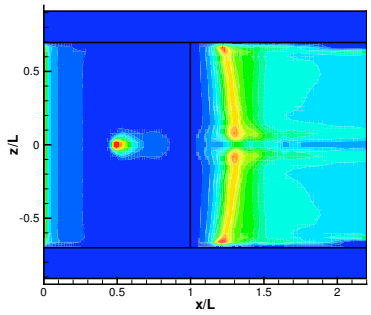

(f) Phase: 100%

Figure 4. Heat transfer rate on the plate surface. Contours: $0.002 \leq C_h \leq 0.028$**.**

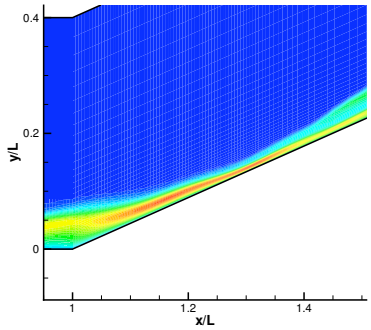

(a) Phase: 0%

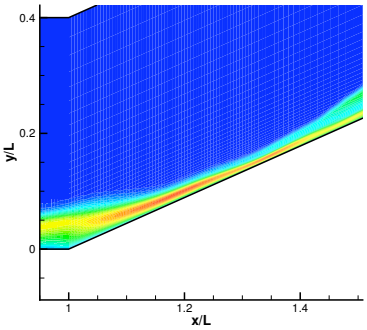

(b) Phase: 20%

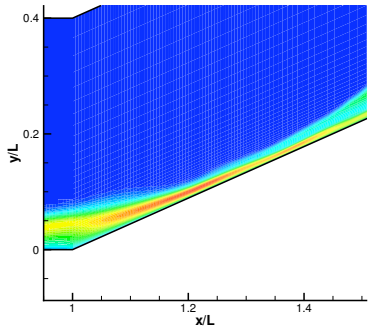

(c) Phase: 40%

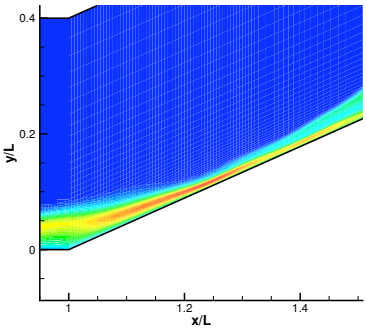

(d) Phase: 60%

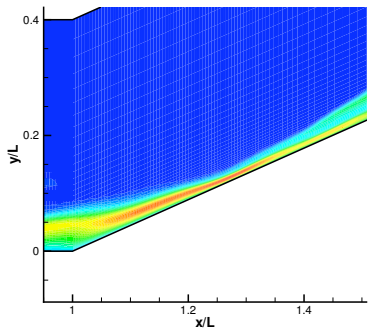

(e) Phase: 80%

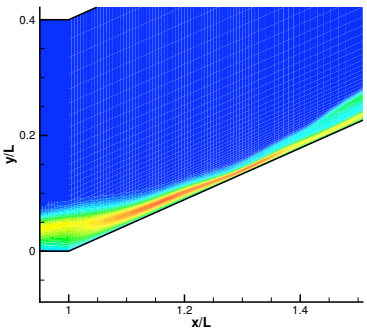

(f) Phase: 100%

Figure 5. Static temperature in the symmetry plane. Contours: $2 \leq T/T_\infty \leq 24$**.**